ADVANCED MATERIALS
www.advmat.de

Quantum Advantage in a Molecular Spintronic Engine that Harvests Thermal Fluctuation Energy

*Bhavishya Chowrira, Lalit Kandpal, Mathieu Lamblin, Franck Ngassam, Charles-Ambroise Kouakou, Talha Zafar, Damien Mertz, Bertrand Vileno, Christophe Kieber, Gilles Versini, Benoit Gobaut, Loïc Joly, Tom Ferté, Elmer Monteblanco, Armel Bahouka, Romain Bernard, Sambit Mohapatra, Helena Prima Garcia, Safaa Elidrissi, Miguel Gavara, Emmanuel Sternitzky, Victor Da Costa, Michel Hehn, François Montaigne, Fadi Choueikani, Philippe Ohresser, Daniel Lacour, Wolfgang Weber, Samy Boukari, Mebarek Alouani, and Martin Bowen**

Recent theory and experiments have showcased how to harness quantum mechanics to assemble heat/information engines with efficiencies that surpass the classical Carnot limit. So far, this has required atomic engines that are driven by cumbersome external electromagnetic sources. Here, using molecular spintronics, an implementation that is both electronic and autonomous is proposed. The spintronic quantum engine heuristically deploys several known quantum assets by having a chain of spin qubits formed by the paramagnetic Co center of phthalocyanine (Pc) molecules electronically interact with electron-spin-selecting Fe/C_{60} interfaces. Density functional calculations reveal that transport fluctuations across the interface can stabilize spin coherence on the Co paramagnetic centers, which host spin flip processes. Across vertical molecular nanodevices, enduring dc current generation, output power above room temperature, two quantum thermodynamical signatures of the engine's processes, and a record 89% spin polarization of current across the Fe/C_{60} interface are measured. It is crucially this electron spin selection that forces, through demonic feedback and control, charge current to flow against the built-in potential barrier. Further research into spintronic quantum engines, insight into the quantum information processes within spintronic technologies, and retooling the spintronic-based information technology chain, can help accelerate the transition to clean energy.

1. Introduction

Classical engines convert heat into work by transferring heat from hot to cold thermal baths using a working substance (WS) that is sequentially put into contact with each bath. This upstream flow of heat thermodynamically increases the engine's entropy. During this process, nature limits the engine's maximum efficiency, which cannot surpass an ideal value determined by the ratio of the temperatures of the two baths. This limit, proven by Carnot in 1824, embodies the second law of thermodynamics.

Quantum engines can surpass this limit by retooling its underlying concepts. Both theory[1–4] and experiments[3,5–7] suggest that additional work capacity, called "ergotropy", can be harvested from quantum systems. In theory, the operation of these engine can be separated into "strokes" that emulate Nature's principle of least action.[3] A stroke's action is characterized by its duration and the rate

B. Chowrira, L. Kandpal, M. Lamblin, F. Ngassam, C.-A. Kouakou, T. Zafar, D. Mertz, C. Kieber, G. Versini, B. Gobaut, L. Joly, T. Ferté, R. Bernard, S. Mohapatra, E. Sternitzky, V. Da Costa, W. Weber, S. Boukari, M. Alouani, M. Bowen
Institut de Physique et Chimie des Matériaux de Strasbourg
UMR 7504 CNRS
Université de Strasbourg
23 Rue du Lœss, BP 43, Strasbourg 67034, France
E-mail: martin.bowen@ipcms.unistra.fr

The ORCID identification number(s) for the author(s) of this article can be found under https://doi.org/10.1002/adma.202206688.

DOI: 10.1002/adma.202206688

B. Chowrira, F. Choueikani, P. Ohresser
Synchrotron SOLEIL
L'Orme des Merisiers
Saint-Aubin, BP 48, Gif-sur-Yvette 91192, France

B. Vileno
Institut de Chimie
UMR 7177 CNRS
Université de Strasbourg
4 Rue Blaise Pascal, CS 90032, Strasbourg 67081, France

E. Monteblanco, M. Hehn, F. Montaigne, D. Lacour
Institut Jean Lamour UMR 7198 CNRS
Université de Lorraine
BP 70239, Vandœuvre les Nancy 54506, France

A. Bahouka
IREPA LASER
Institut Carnot MICA
Parc d'innovation – Pole API, Illkirch 67400, France

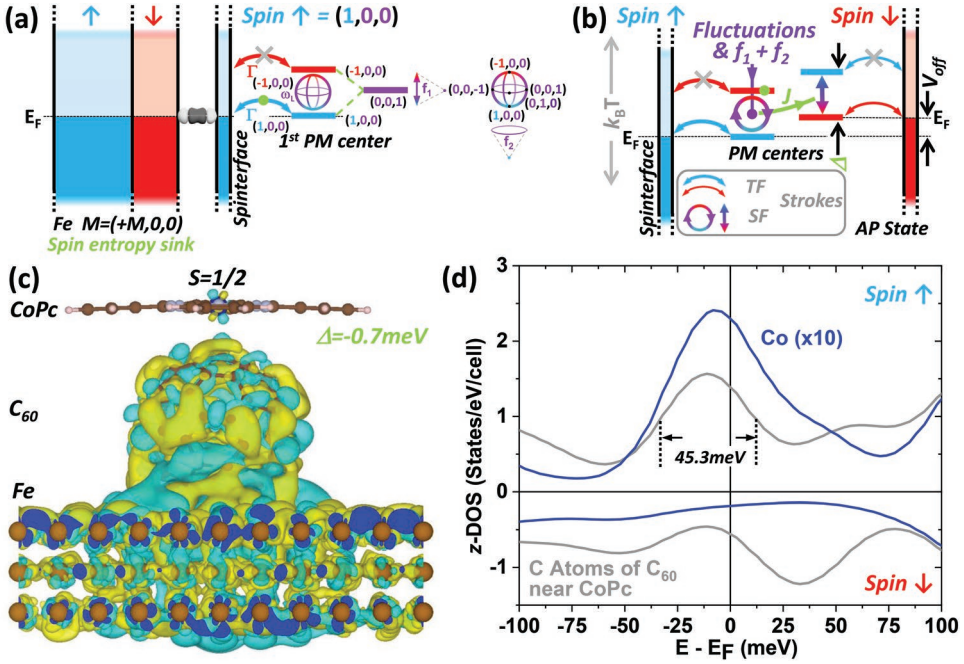

Figure 1. A molecule-based spintronic quantum engine. a) Density of states schematic: spintronic implementation of the transport fluctuation (TF) stroke between the device electrode in its FM ground state and the spin states of the working substance (WS)'s nearest PM center, mediated by a spinterface with full transport spin polarization. Quantum coherence and decoherence processes on the WS are shown. b) This stroke appears in the overall engine schematic that also shows the spin flip (SF) strokes on a PM center's spin states, and between the PM centers forming the WS, against thermal fluctuations for $k_BT > \Delta$. Quantum assets are color-coded in green in (a) and (b). See main text for details. c) Spatial charge-transfer maps across Fe/C_{60}/CoPc reveal sizeable hybridization on C_{60} (i.e., the spinterface) and electron tunneling between C_{60} and CoPc across an antibonding state. Green/cyan isocontours depict charge gain/loss of 0.0007 e Å^{-3} The antiferromagnetic case is shown. d) The antibonding state's density of states around E_F reveals how the Co d_{z^2} and C p_z orbitals share a spectral feature that appears only in the spin ↑ band. This illustrates the high spin polarization and bandwidth of the TF stroke (see (a)).

at which it couples the WS to the baths. If the engine's baths and WS are endowed with quantum properties, they can constitute quantum assets (QAs)[1–4,7] that promote the storage and transfer of ergotropy.

So far, the only engines to implement a quantum advantage have coherently manipulated an atomic WS using 1–10 MHz strokes[3,5–7] using microwave or laser external sources, i.e., the engine isn't autonomous. Conversely, despite much faster 2–10 GHz electronic strokes, on-chip electronic engines[8,9] have so far exhibited sub-Carnot efficiencies due to mesoscopic WSs that are much more prone to quantum decoherence.

We propose spintronics[10] as a potent scientific and industrial platform to achieve an electronic autonomous engine with a quantum advantage, and augment our prior spintronics-only description[11] with concepts drawn from quantum thermodynamics.[1–7,12–15] The system under study (see Experimental Section) is a molecular device in which electronic interactions occur between the spin states of paramagnetic (PM) Co centers borne by phthalocyanine molecules (CoPc), which form the engine's WS, and those of ferromagnetic Fe electrodes (see **Figure 1**a). Ultrathin C_{60} intercalation layers ensure not only a spin selectivity[16] of these electronic interactions, but a partial magnetic decoupling[17] between Fe and Co spins, such that the Co spins may fluctuate in an effective magnetic field[11] that lifts the spin degeneracy by Δ (Figure 1a,b). The resulting coherent superposition of spin states can constitute a QA (green dashed lines of Figure 1a) if the spin population is inverted.[3]

Our engine operates by harvesting the energy of these thermal fluctuations using electronic transport across the Fe/C_{60} interface. Indeed, this so-called "spinterface"[16] involves a low density of electron states with narrow energy width and high transport spin polarization. These properties enable the spinterface to electronically interact as a non-thermal bath[2,18,19] with the WS, i.e., constitute a QA (green dot in Figure 1a). Furthermore, magnetic superexchange interactions[20] with energy J between the PM Co atoms of the WS promote a $S = 1/2$ molecular spin chain. This means that the spin coherence between the WS's spin states can be thermally driven through a magnetic phase transition, and dynamically modified by the electronic interaction with the non-thermal baths (Figure 1c,d). This constitutes another QA.[18] In our design, the different thicknesses of the C_{60} intercalation layers promote different transmissions of spin-conserved transport between the WS and each spinterface. This helps to break the detailed balance of charge-transport fluctuations, leading to a preferred one-way direction of current. Overall, our engine's operation involving several QAs differs from the spin-based classical thermoelectric effects of spin caloritronics.[21]

H. Prima Garcia, S. Elidrissi, M. Gavara
Instituto de Ciencia Molecular (ICMol)
Universidad de Valencia
Catedrático Jose Beltrán 2, Paterna 46980, Spain

Thus, the quantum advantage we claim to observe heuristically originates from this tailored electronic interaction between the FM thin film and the discrete spin states of the PM centers. Our spintronic quantum engine transforms the thermal energy of spin fluctuations on the WS's PM centers into a directed dc current by rectifying the resulting transport fluctuations between the WS and the device electrodes. After presenting our experimental results, we will propose a more detailed description of the engine's operation, several aspects of which mimic that of a quantum measurement engine.[4]

2. Transport Experiments

Our nanoscale vertical junctions (see Experimental Section) exhibit a large persistent non-zero spontaneous current $I_{Sp} \approx -10$ µA (see **Figure 2**a for nanojunction A, and Figure S3 (Supporting Information) for other junctions) that is two orders of magnitude larger than the experimental offset (see Note S2 (Supporting Information) on control experiments). Its amplitude is not strongly affected by intermittent sweeps of an external magnetic field up to 2 T applied perpendicularly to the electrode magnetizations. This confirms that, in our implementation, the engine's primary energy source is not the external applied magnetic field.[22] We present in Figure 2b repeated $I(V)$ sweeps at 240 K, from which we infer a slope resistance around $V = 0$ of $R_s = 157\ \Omega$. From $I_{Sp}(t)$ (see top inset), we find at $V = 0$ that the offset current $I_{Off} = -26$ µA $= I_{Sp}$. This suggests that, once a bias voltage V has been applied, and on the timescale of hours, applying $V = 0$ does not confer energy to the device. I_{Off} and the bias offset $V_{Off} = 4.05$ mV at $I = 0$ (see top inset), are respectively 230× and 100× larger than the experimental offset errors observed for a 100 Ω calibrated resistance (magenta crosspoint in Figure 2b and Note S2, Supporting Information).

The lower inset of Figure 2b reveals a slight, hysteretic deviation from a linear response that depends on the sweep direction (red and blacks arrows). Within this 1.4 mV bias window, the numerical derivative (see Figure 2c) reveals features with an energy width as low as 0.3 meV despite an expected thermal smearing of 2–3 k_BT upon transport, with $k_BT = 20.7$ meV here. This sub-k_BT spectral resolution is mostly unchanged upon reducing thermal fluctuations by a factor of 6, as are the main spectral features (denoted A, B and C in Figure 2d). This 1.4 meV window likely defines[11] the energy range that contains those spin states of the working substance that are involved in the engine's operation. The persistence of these features with sub-k_BT spectral width above the dissipation threshold induced by thermal fluctuations is most likely a result of feedback-induced

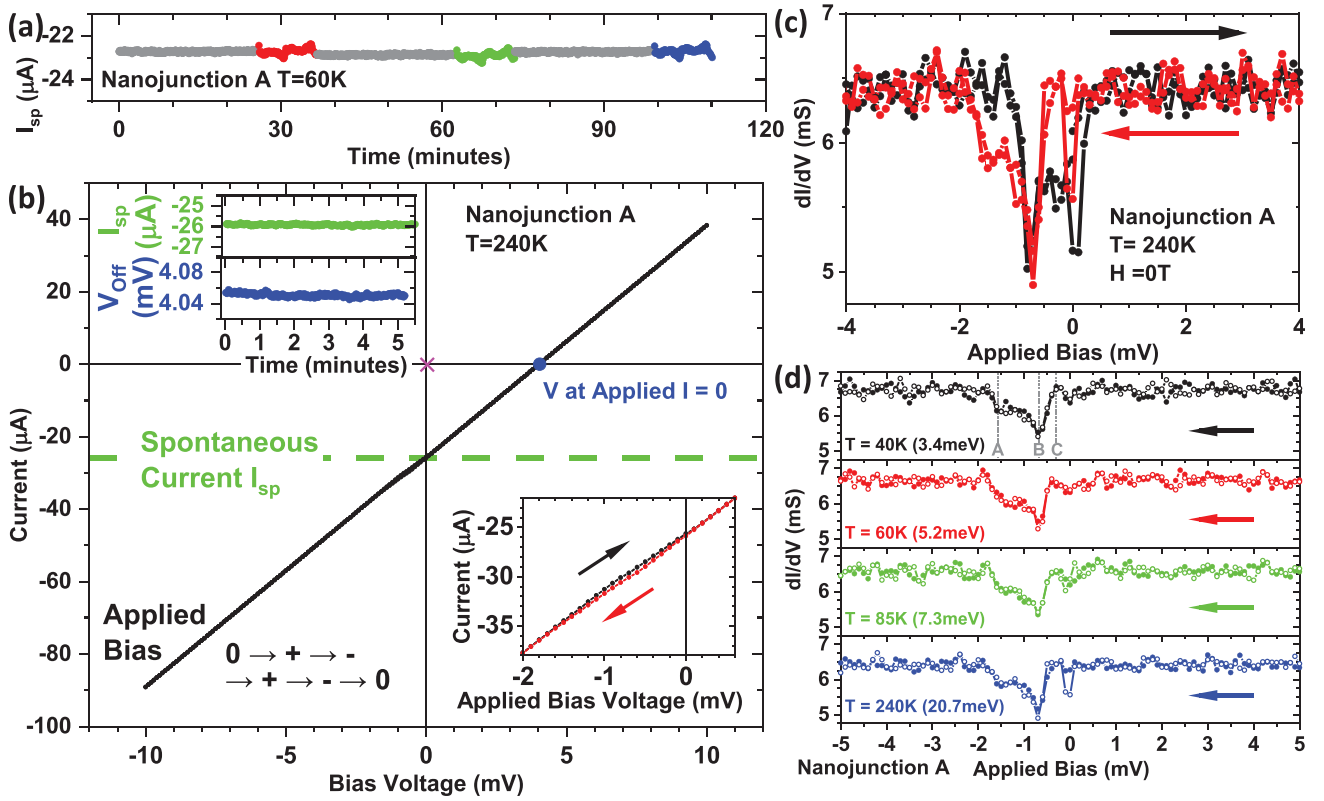

Figure 2. Long-lived spontaneous electrical signals. Data on metallic nanojunction A: a) time dependence of I_{sp} at $H = 0$ (gray) and upon applying an H field (red, green, blue) orthogonal to the electrode magnetizations. b) $I(V)$ data at 240 K. The magenta crosspoint represents the experimental (V,I) error. The top insets show the time dependence of I_{sp} and V_{Off}, while the zoom around $V = 0$ (lower inset) reveals an $I(V)$ hysteresis that contains features with a sub-$k_B T$ spectral resolution in (c) the current derivative dI/dV. Forward (black) and return (red) traces are shown. d) Return dI/dV traces for 40 K, 60 K, 85 K and 240 K reveal essentially identical features with a sub-k_Bi spectral resolution, i.e., the thermodynamical signature of a quantum asset.

noise reduction[23] and should therefore constitute the quantum thermodynamical signature of a non-thermal bath interaction within the engine operation.

Due to discrete states within the barrier,[24] spintronic regimes involving multiple metallic and semiconducting transport nanochannels may coexist[25] in a device. The slight decrease in junction conductance with increasing temperature (see Figure 2d) confirms the metallic nature of nanojunction A. This, and several other metallic nanojunctions, exhibit a maximal output power P_{Max} such that $17 < P_{Max}$ (nW) < 55 for $150 < R_s$ (Ω) < 800 at 40 K. We now turn to semiconducting nanojunction B, for which we observe (see **Figure 3**a) a mostly linear $I(V)$ at 360 K (R_s= 1.05 kΩ) that becomes increasingly non-linear as T is lowered to 40 K (R_s= 25.9 kΩ). The apparent common crosspoint of $I(V,T)$ data (inset of Figure 3a) is orders of magnitude beyond measurement artefacts (see magenta crosspoint and Note S2, Supporting Information) and might reflect a bias-induced symmetrization of the spin potential landscape against thermal broadening effects.[11] We observe P_{Max} = 450 nW at 40 K (Figure 3a inset). This represents a 450× increase over the previous record measured at 3 K and H = 1 T,[22] and at 295 K a 270× improvement.[11] At 360 K, we still observe P_{Max} = 24 nW, which is promising for applications. Our results thus not only dwarf those from possibly similar experiments,[11,22,26] but also those from mesoscopic quantum heat engines.[8]

As seen in the ln vs $1/T$ plots in Figure 3b, the R_s data follows $R_S = R_0 e^{-E_a/k_B T}$ with a single thermal activation energy E_a over $40 < T$ (K) < 360. In contrast, V_{Off} and P_{Max} both exhibit two thermal activation regimes. We observe a ≈3× increase in E_a from the low T to the high T regime. This could reflect hopping transport[27] for $T > 120$K between spins onto and along the three member-long chain. As a corollary, coherent spin-polarized transport across the spin chain would occur for $T < 120$K. This suggests that the structural arrangement[20] of the CoPc spin chain in the junction's effective nanotransport path[28] yields a magnetic exchange energy J such that $k_B T_c = J$ with T_c = 120 K. Considering that $10 < T_c$ (K) < 400 theoretically,[20] this is compatible with prior reports for Pb//CoPc (T_c = 105 K)[29] and CoPc on Fe (T_c = 72 K)[17] around the stable bulk α-CoPc phase (T_c = 86 K).[20]

To independently determine T_c for CoPc on C_{60} in our nanojunction stack, we performed electron paramagnetic resonance (EPR) measurements on a C_{60}/CoPc multilayer stack (see Experimental Section and Note S3, Supporting Information, for additional details). Referring to Figure 3c, we observe a radical peak centered around the Landé g-factor $g = 2$. We also observe 8 oscillations on either side of the radical peak. Using reference samples and simulations (see Note S3, Supporting Information), we attribute the radical peak to Kapton and to C_{60}, and each set of 8 oscillatory features to the hyperfine structure of a paramagnetic center around a Co nucleus with nuclear spin 7/2. Upon subtracting the simulated Kapton and C_{60} contributions

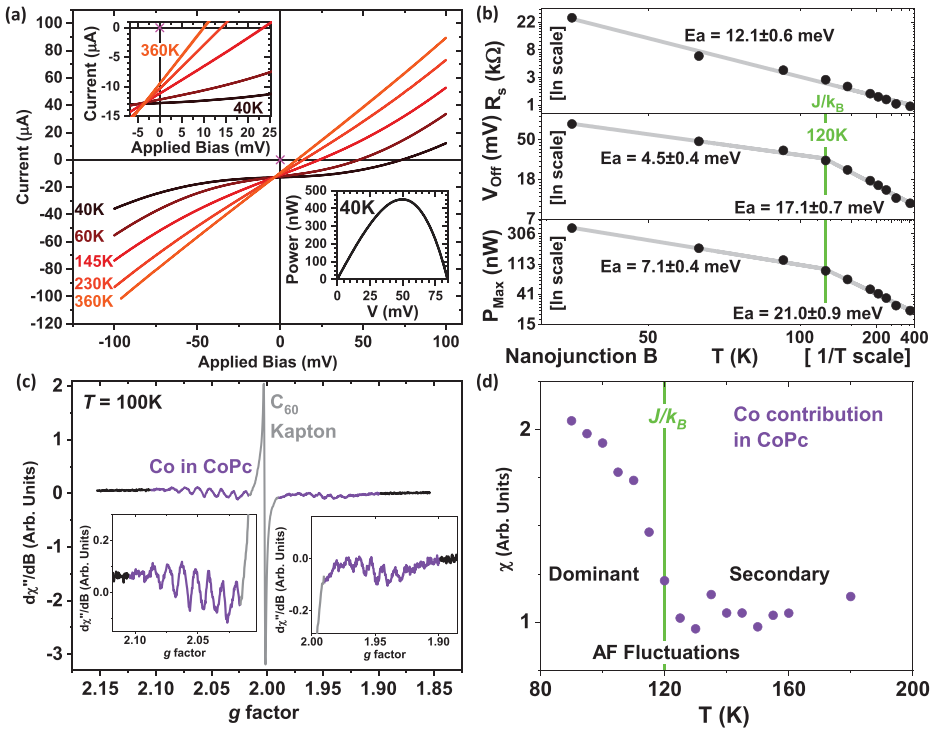

Figure 3. Thermally activated electrical power across a magnetic phase transition. a) $I(V)$ data from nanojunction B at $H = 0$ T within $40 < T$ (K) < 360. Top inset: zoom at low bias. Bottom inset: $P(V)$ data showing P_{Max} = 450 nW at 40 K. The magenta crosspoint is the experimental error (see Experimental Section). b) ln vs $1/T$ plots of (top) R_s, (middle) V_{Off} and (bottom) P_{Max}. P_{Max} decreases from 370 nW at 40 K to 24 nW at 360 K per two thermal activation regimes, with a 120 K crossover temperature. The activation energy E_a is given for each regime. c) EPR spectrum at T = 100 K. The color-coded feature identification is described in Note S3, Supporting Information. Insets: zoom on the Co contribution from CoPc. d) Temperature dependence of the Co contribution in CoPc to the EPR Intensity. A signal increase is observed for $T < 120$K.

from the main EPR dataset, we obtain the temperature dependence of the Co contribution in CoPc (see Figure 3d). The Co EPR signal exhibits a clear increase for $T < 120$ K, as expected when, below the magnetic phase transition at T_c, AF-correlated spin fluctuations along an spin chain of odd length dominate thermal disorder. As a quantum thermodynamical signature, we thus confirm that the magnetic phase transition of the WS plays a role in the spintronic engine's performance, as expected of this QA.[18]

To confirm these devices' spintronic underpinnings, the $I(H)$ data at 40 K from nanojunction C in **Figure 4**a reveal a strong in-plane H dependence of junction current, which saturates for $|H| > 0.5$ T (see Note S4, Supporting Information) upon achieving the parallel orientation of FM electrode magnetization. The current can be suppressed at $H = 0$ and $H = -0.5$ T for $V_{Off} = 2.76$ mV and $V_{Off} = 2.13$ mV, respectively. Thus, the junction's two magnetic states promote differing V_{Off} . They also drive a sign change in current at $V = 2.67$ mV, with $I = \pm 1$ µA. These (V,I) pairs lie well beyond possible experimental offsets (see Note S2, Supporting Information). The $I(V)$ data of Figure 4b confirms these (V,I) pairs. From $R_S(0\ T) = 63\ \Omega$ and $R_S(-0.5\ T) = 550\ \Omega$, we observe a magnetoresistance $MR = \frac{R_S(0\ T)}{R_S(-0.5\ T)} - 1 = -89\%$ (bounded by –100% for full spin polarization of the current). Using $I(H)$ data from panel (a), we plot $R_S(H)$ in Figure 4c, and again obtain MR = –89%. Consistency between these three data panels is visualized by blue crosses in panels (b) and (c). The MR = –89% translates into an "optimistic" magnetoresistance $MR' = \frac{R_S(-0.5\ T)}{R_S(0\ T)} - 1 = 770\%$. This implies[10] an average transport spin polarization $P = 89.1\%$ of the two Fe/C_{60} spintronic selectors.[16] The magnetocurrent $MC = \frac{I(-0.5\ T)}{I(0\ T)} - 1$ reaches –100% and 1470% at each spintronic V_{Off} . This showcases this device class as a spintronically controlled switch of current direction and flow.

3. Model

In the context of these experimental datasets, we now propose a basic description of how quantum assets heuristically drive the spintronic engine's operation, and utilize density functional theory to support our claim of spinterface-driven spin coherence on the WS's Co sites, in view of the long-lasting dc currents that were observed. Referring to Figure 1a, the $(+M,0,0)$ magnetic orientation of the Fe layer sets a spin referential for other electronic interactions, starting with the spin-polarized charge transfer toward adjacent C_{60} molecules. This generates the spinterface electronic state described previously, which can be seen as a magnetic quantum dot.[11] Prior to any electronic interaction, the Co atom on the phthalocyanine molecule bears an energetically degenerate $S = 1/2$ spin on the d_{z^2} orbital $((x,y,z) = (0,0,\pm 1)$ on the Bloch sphere, see Figure 1a).

The electronic interactions between the FM electrode and PM centers across the spinterface lift this degeneracy by Δ and describe the engine's spin-conserved transport fluctuation (TF) stroke. The forward TF stroke from the FM electrode to the nearest PM center on the chain is mediated by the spinterface's full spin polarization along the (1,0,0) direction. This imposes the injection into the WS of coherent spins along (1,0,0), against the WS's decoherence processes (in purple in Figure 1a,b).

The reverse TF flow of current also requires that the spin on the WS be (1,0,0). This not only constrains the possible channels of spin decoherence for the WS's spins (Figure 1a), but also describes an autonomous measurement of the WS state, i.e., the QA of a quantum measurement engine.[4] The spinterface acts as an autonomous Maxwell demon[30] that gains information on the WS and uses it as feedback to control the electron transfer rate across the barrier. Overall, these TFs generate resistive losses due to spin scattering between the spinterface and the FM film with very different spin polarizations. This rise in spin-based entropy of the FM essentially embodies the Landauer principle:[31] the quantum information gained by the measurement of the WS's spin state[4] is erased as the FM thin film scatters the excess spin. We believe that, importantly, the Fe FM thin film synergistically sinks this spin entropy by returning to the stable FM ground state with lower spin disorder.[32]

These features of the TF stroke require: 1) the presence of magnetic coupling across C_{60} between Fe and the nearest Co site of the WS; and 2) a stroke frequency that is much greater than that of the WS's decoherence processes. To qualitatively characterize these aspects of our experiment's TF stroke, we

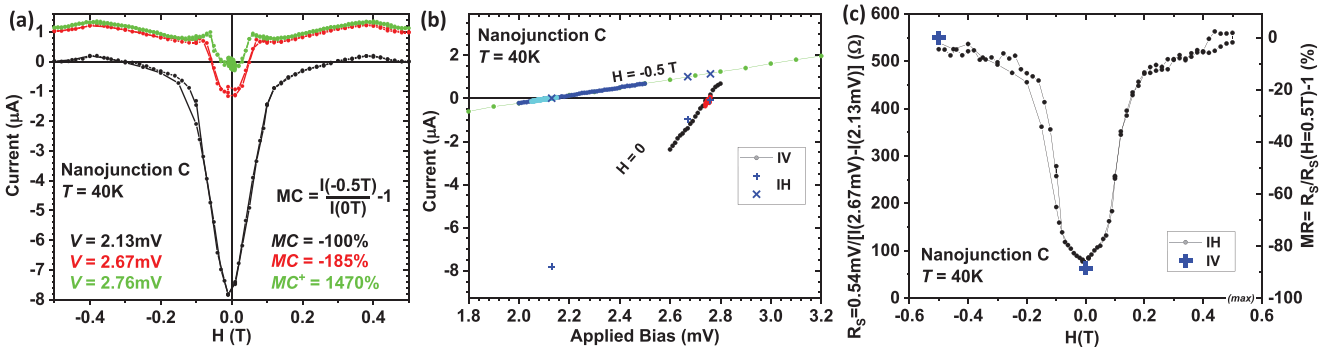

Figure 4. Spintronic features of the thermal energy harvester. a) $I(H)$ data acquired on nanojunction C at 40 K. b) $I(V)$ data at $H = 0$ T and $H = -0.5$ T, revealing a linear behavior with $R_S = 63\ \Omega$ and $R_S = 550\ \Omega$ around $V_{Off} = 2.13$ mV and $V_{Off} = 2.76$ mV, respectively. The blue crosses reflect the $I(H)$ data from (a). c) $R_S(H)$ calculated from two $I(V_0,H)$ datasets from (a). The blue crosses indicate R_S inferred from (b). The two spintronic V_{Off} lead to extremal values MC (%) in $I(H)$ data, as do the two spintronic R_S regarding $-100 < MR\ (\%) < \infty$.

computed the electronic interactions (see Theoretical Section) across the bcc Fe(110)/C_{60}(1 ML)/CoPc(1 ML) system (ML = monolayer). We observe a charge transfer of 1.231e^- from Fe that is delocalized onto C_{60} (Figure 1c). A much weaker 0.03e^- transfer from C_{60} to CoPc occurs across an antibonding state. This tunneling-mediated electronic interaction results in spectral features across E_F that are shared both by the Co d_{z^2} orbitals of CoPc and the p_z orbitals of the neighboring C sites of C_{60} only for spin ↑ electrons (Figure 1d).[33] These interactions result in a lifting of the Co spin degeneracy by Δ = 0.7 meV according to our DFT calculations (see Figures 1b,c and Experimental Section). This effective magnetic field H = 6 T, generated by spintronic anisotropy,[11] is much stronger than that for a noble-metal spacer[34] because it originates from C_{60}-mediated Fe–Co antiferromagnetic superexchange.[35]

The TF strokes quantum correlate the spinterfaces with the endmembers of the WS's spin qubits borne by 1D molecular chains, thereby imposing boundary conditions on the WS. Each member of the spin chain is coupled to its two neighbors by magnetic exchange with characteristic energy J.[20] The WS has an antiferromagnetic ground state that is promoted by this coupling, and is reinforced when the two FM electrodes are antiparallel-oriented. Flipping one spin on the chain promotes an excited state that contains ergotropy. Since the WS is a quantum system with a reduced number of discrete energy levels, it can therefore exist in a quantum coherent superposition of states,[4,15] and its temperature is not well defined when isolated. The WS is coupled to the Fe electrode via the spinterface acting as a non-thermal bath with temperature T. The 45.3 meV width of the electronic interaction (Figure 1d) suggests that at least these endmembers remain quantum coherent with the spinterfaces up to k_BT = 45.3 meV. This would explain the persistence of power output for $k_BT > J$, in line with the presence of quantum correlations above the critical point of a 2nd order phase transition. Indeed, the loss of correlations in the spin fluctuations along the molecular chain for $k_BT > J$ is valid for a macroscopic, statistical ensemble (e.g., in our EPR experiment). However, these correlations may persist within a single chain along the device's nanotransport path.[17,28] It is also possible that quantum steering[7] plays a role here. Furthermore, when $k_BT < J$ and T is further lowered, an additional source of coherence is provided by the increased predominance, against thermal energy, of the antiferromagnetic interaction between the WS's spin qubits.

During the engine's so-called spin-flip (SF) stroke, the thermal fluctuations on and between the PM centers supply magnetic energy to the WS (i.e., charging), which will be extracted during the TF stroke via an ergotropic return from a non-passive (i.e., excited) state to the ground state.[30] Indeed, although stochastic in origin, these fluctuations can provide QAs by inducing coherence[1] and by energetically pumping the superposition of quantum states.[3] SF operations between qubits[4,5] are also responsible for flipping the spin on the chain endmember prior to the TF stroke (e.g., from (1,0,0) to (–1,0,0) in Figure 1a). The TF stroke thus drives electronic-transport processes across the device, and electronically connects the WS with the spinterface non-thermal baths. This spintronic passivation effect enables the extraction of thermal energy and causes a directed current to flow. This asymmetric regime of operation is enabled by the structural/electronic asymmetries of our device, in this case thanks to different C_{60} thicknesses (thick and thin transmission arrows in Figure 1b). This generates different TF stroke frequencies and different spin-splitting values Δ on each PM center. This asymmetrizes the SF stroke frequency along the WS's qubits.

To provide a basic justification for this engine's operation, we establish order-of-magnitude comparisons between the frequency of the TF and SF strokes, against the frequencies of the WS's spin-charge and spin-lattice decoherence processes,[36] which occur along (0,±1,±1) (in purple in Figure 1a,b). For CoPc, the respective frequencies at 7 K are f_1 = 1 kHz and f_2 = 1 MHz,[36] noting that f_2 can increase ≈100× at 300 K.[37] For $k_BT \geq \Delta$, and given Δ = 0.7 meV, the SF stroke cutoff f_{SF}= 169.5 GHz. Finally, according to the Heisenberg uncertainty principle, the 45.3 meV minimum energy width of the TF stroke's spectral features (Figure 1d) corresponds to an attempt frequency $f_{TF} = 1.38 \times 10^{14}$ Hz. This suggests[38] that f_1, $f_2 << f_{TF}$, f_{SF} throughout our experiments at 40 < T (K) < 360. This would provide the necessary speed of the engine's cycle to overcome all decoherence processes, even at room temperature as seen experimentally.[39] As a QA,[13] the TF stroke implements the quantum Zeno effect during the engine operation, i.e., it repeatedly sets and measures the WS's quantum thermodynamical state. This ultrafast dynamic stabilizes the spin chain against decoherence.

As calls for a quantum energy initiative grow,[40] our results introduce spintronics[10] onto the quantum technologies roadmap as a very promising platform to implement energy applications of autonomous quantum engines, and raise interesting questions for further research. A current can drive the electronic properties of paramagnetic centers: temperature, exchange coupling and even entropy production close to a phase transition without a temperature gradient.[11,41,42] Does this engine require electrical priming to operate, i.e., is it a quantum battery?[6,13] Can precise thermometry confirm the entropy sinking[32] by the FM state of the electrodes? Can certain aspects such as TF stroke asymmetry,[14] exchange coupling[20] or number/parity of qubits be optimized, e.g., using molecular engineering? Does zero-point energy play a role? Answering these questions, for example using in operando electron spin resonance, would shed insight into the autonomous engine's multiple interlocking quantum resources, and help to determine its efficiency. Looking ahead, the most promising vector to industrialize this quantum technology could be MgO spintronics,[11] which so far has mostly targeted information storage and processing needs.[10] To transform it into a dual-use information/energy technology workhorse will require mastering the insertion of paramagnetic centers,[11] most likely through the control of oxygen vacancies.[24] Harvesting/storing this most basic form of energy—ambient thermal energy, could help to alter our nomadic energy needs and accelerate the transition to clean energy.

4. Experimental Section

Device Preparation: Si/SiO_x//Cr(5)/Fe(50)/C_{60}(n ML)/CoPc(3ML)/C_{60}(5ML)/Fe(10)/Cr(50) heterostructure stacks were grown in situ and

at room temperature in an ultrahigh vacuum multichamber cluster by dc sputtering (metals) and thermal evaporation (CoPc). All numbers are in nm; 1 ML C_{60} = 0.9 nm. 1 ML CoPc = 0.4 nm. The SiO_x substrate was annealed at 110 °C and allowed to cool down prior to deposition. Metals were sputtered in an Ar pressure $P = 1.5 \times 10^{-3}$ mbar (Cr) and $P = 6 \times 10^{-4}$ mbar (Fe). Molecules were thermally evaporated under $P = 3 \times 10^{-9}$ mbar. The C_{60} thickness n for nanojunctions A, B, and C was 3, 1, and 1 ML, respectively. The Fe layers are in-plane magnetized. Nanojunctions were crafted[17] using 300 nm-diameter SiO_2 nanobeads thanks to a recently developed resist- and solvent-free nanojunction process, and were wirebonded to a sample chip. The positive contact was connected to the junction's top electrode. All data were acquired with the sample at a constant, nominally uniform temperature T.

EPR Sample Preparation: A Kapton (25 µm)//C_{60} (6 ML)/[CoPc (3 ML)/C_{60} (6 ML)]$_{300}$/C_{60} (18 ML)/MgO (30 nm) sample was grown under UHV conditions. The Kapton substrate was annealed at 110 °C and allowed to cool down prior to deposition. MgO was rf-sputtered from a MgO target at a Ar pressure of 1.5×10^{-3} mbar. Molecules were thermally evaporated under $P = 3 \times 10^{-9}$ mbar. Under ex situ conditions, the sample was cut into strips and inserted into a quartz tube. After flushing with He, the tube was sealed at a He pressure of 500 mbar and inserted into the EPR cryostat. See Note S3, Supporting Information, for more experimental details.

5. Theoretical Section

The structural and magnetic properties of the bcc Fe(110)/C_{60}/CoPc system were calculated using density functional theory (DFT) by means of the Vienna Ab Initio Simulation Package (VASP) and its built-in projector augmented wave (PAW) pseudopotentials. The exchange and correlation potentials are within the generalized gradient approximation (GGA) as parametrized by Perdew, Burke, and Ernzerhof. The van der Waals (VdW) weak interactions were computed within the GGA-D3 approach developed by Grimme and later implemented in the VASP package. A kinetic energy cutoff of 450 eV was used for the plane-wave basis set. To include the correlation effects of transition-metal 3*d* electrons, we adopted the Dudarev et al.[43] DFT-GGA+U method, using a Hubbard U of 5 eV and an exchange parameter J of 1 eV, which amount to an $U_{eff} = U - J = 4$ eV. This value of U_{eff} was found by Brumboiu et al.[44] to produce the best description of the HOMO–LUMO gap of CoPc, its Co magnetic moment, its vibrational frequencies, as well as its valence-band photoelectron spectra as compared to experiment and hybrid functional calculations. The supercell geometry comprises the following three Bravais vectors: (22.96 Å, 0, 0), (14.35 Å, 20.29 Å, 0), and (0, 0, 37 Å), using 80 iron atoms per layer in the bcc structure along (110). The vacuum region separating the periodic images is 25 Å.

To confirm the presence of magnetic coupling between Fe and Co, and to estimate the electronic bandwidth, we adopted a standard molecular geometry (see Figure 1c) as studied elsewhere,[45] assuming that only C_{60} is experimentally present at the Fe interface. Using this educated guess, atomic positions were relaxed by annulling the force on the atoms to within 10^{-4} meV Å^{-1}. First, using several structural models, we relaxed the subsystem composed of 3 layers of Fe(110) and C_{60} to find the equilibrium distance. Then, using several structural models, we optimized the CoPc–C_{60} distance to find the ground state. We then used these configurations to study the magnetic state of the entire Fe(110)/C60/CoPc system. To this end, we considered both ferromagnetic and antiferromagnetic couplings between the Co of CoPc and Fe(110). After atomic relaxations, we found that the antiferromagnetic configuration is more stable by ≈–0.7 meV. This ground state becomes more robust (–7.8 meV) when 5ML of Fe are used but the changes in the density of states and the electron transfer are negligible. The C_{60}–Fe(110) distance is about 2.26 Å, and that between C_{60} and CoPc is 2.6 Å. In both magnetic states, the magnetic moment of the iron atoms below the C_{60} molecule is 2.29 μ_B, and is 2.72 μ_B far from C_{60}. The magnetic moment of Co in CoPc is +1.34 μ_B (FM coupling) and –1.34 μ_B (AFM coupling). The magnetic moment on the CoPc ligands is –0.082 μ_B (FM coupling) and +0.089 μ_B (AFM coupling).

Supporting Information

Supporting Information is available from the Wiley Online Library or from the author.

Acknowledgements

The authors thank J. Arabski for invaluable support with sample growth, R. Whitney, Ph. Turek, and Y. Henry for stimulating discussions, B. Doudin for collaborating on nanobead processing, the remaining members of the STNano technological platform staff for technical assistance with certain processing steps, and the IPCMS machine shop for support.[46] Work was performed using Synchrotron SOLEIL beamtime proposals 20170317 and 20180169. The authors acknowledge financial support from the Region Grand Est and Synchrotron SOLEIL, from CEFIPRA grant 5604-3, from the ANR (ANR-06-NANO-033-01, ANR-09-JCJC-0137, ANR-14-CE26-0009-01, ANR-21-CE50-0039), the Labex NIE "Symmix" (ANR-11-LABX-0058 NIE), the ITI QMat "SpinDrive", the EC Sixth Framework Program (NMP3-CT-2006-033370), the Contrat de Plan Etat-Region grants in 2006 and 2008, by "NanoTérahertz", a project co-funded by the ERDF 2014–2020 in Alsace (European Union fund) and by the Region Grand Est through its FRCR call, by the impact project LUE-N4S part of the French PIA project "Lorraine Université d'Excellence", reference ANR-15IDEX-04-LUE and by the FEDER-FSE "Lorraine et Massif Vosges 2014–2020", a European Union Program. The computation was performed using HPC resources from GENCI-CINES Grant gem1100 and the HPC supercomputer of the University of Strasbourg. Financial support from the IR INFRANALYTICS FR2054 for the EPR investigations is gratefully acknowledged.

Conflict of Interest

The authors declare no conflict of interest.

Authors Contributions

B.C. and L.K. contributed equally to this work. M.B. conceived the experiment. B.C., C.K., and V.d.C. grew the transport samples, with help from G.V. and B.G.; L.K. made the nanojunctions, with help from D.M., A.B., R.B., and B.C.; B.C., M.B., and L.K. performed measurements with help from L. J., E.M., S.M., E.S, H. P.G., S.E., M.G., F.C., and P.O.; M.B., B.C. and L.K. analyzed the data, with input from M.H., F.M., B.V., D.L., W.W., and S.B.; B.G., W.W., S.B., V.d.C., T.Z., M.L., B.V., and M.B. grew the ESR multilayers; C.-A.K. and B.V. performed EPR experiments and analyzed the data, with input from M.B.; F.N. performed the calculations, with input from M.A. and M.B.; M.B. wrote the manuscript, with help from M.L. and input from all authors.

Data Availability Statement

The data that support the findings of this study are available from the corresponding author upon reasonable request.

Keywords

energy harvesting, molecules, quantum physics, quantum thermodynamics, spintronics

Received: July 22, 2022
Revised: September 25, 2022
Published online: October 31, 2022

[1] M. O. Scully, K. R. Chapin, K. E. Dorfman, M. B. Kim, A. Svidzinsky, *Proc. Natl. Acad. Sci. USA* **2011**, *108*, 15097.
[2] W. Niedenzu, V. Mukherjee, A. Ghosh, A. G. Kofman, G. Kurizki, *Nat. Commun.* **2018**, *9*, 165.
[3] J. Klatzow, J. N. Becker, P. M. Ledingham, C. Weinzetl, K. T. Kaczmarek, D. J. Saunders, J. Nunn, I. A. Walmsley, R. Uzdin, E. Poem, *Phys. Rev. Lett.* **2019**, *122*, 110601.
[4] L. Bresque, P. A. Camati, S. Rogers, K. Murch, A. N. Jordan, A. Auffèves, *Phys. Rev. Lett.* **2021**, *126*, 120605.
[5] J. P. S. Peterson, T. B. Batalhão, M. Herrera, A. M. Souza, R. S. Sarthour, I. S. Oliveira, R. M. Serra, *Phys. Rev. Lett.* **2019**, *123*, 240601.
[6] D. Von Lindenfels, O. Gräb, C. T. Schmiegelow, V. Kaushal, J. Schulz, M. T. Mitchison, J. Goold, F. Schmidt-Kaler, U. G. Poschinger, *Phys. Rev. Lett.* **2019**, *123*, 080602.
[7] W. Ji, Z. Chai, M. Wang, Y. Guo, X. Rong, F. Shi, C. Ren, Y. Wang, J. Du, *Phys. Rev. Lett.* **2022**, *128*, 090602.
[8] M. Josefsson, A. Svilans, A. M. Burke, E. A. Hoffmann, S. Fahlvik, C. Thelander, M. Leijnse, H. Linke, *Nat. Nanotechnol.* **2018**, *13*, 920.
[9] G. Jaliel, R. K. Puddy, R. Sánchez, A. N. Jordan, B. Sothmann, I. Farrer, J. P. Griffiths, D. A. Ritchie, C. G. Smith, *Phys. Rev. Lett.* **2019**, *123*, 117701.
[10] S. Bhatti, R. Sbiaa, A. Hirohata, H. Ohno, S. Fukami, S. N. Piramanayagam, *Mater. Today* **2017**, *20*, 530.
[11] K. Katcko, E. Urbain, B. Taudul, F. Schleicher, J. Arabski, E. Beaurepaire, B. Vileno, D. Spor, W. Weber, D. Lacour, S. Boukari, M. Hehn, M. Alouani, J. Fransson, M. Bowen, *Commun. Phys.* **2019**, *2*, 116.
[12] G. De Chiara, M. Antezza, *Phys. Rev. Res.* **2020**, *2*, 033315.
[13] S. Gherardini, F. Campaioli, F. Caruso, F. C. Binder, *Phys. Rev. Res.* **2020**, *2*, 013095.
[14] P. E. Harunari, F. S. Filho, C. E. Fiore, A. Rosas, *Phys. Rev. Res.* **2021**, *3*, 023194.
[15] M. Josefsson, M. Leijnse, *Phys. Rev. B* **2020**, *101*, 081408.
[16] F. Djeghloul, M. Gruber, E. Urbain, D. Xenioti, L. Joly, S. Boukari, J. Arabski, H. Bulou, F. Scheurer, F. Bertran, P. Le Fèvre, A. Taleb-Ibrahimi, W. Wulfhekel, G. Garreau, S. Hajjar-Garreau, P. Wetzel, M. Alouani, E. Beaurepaire, M. Bowen, W. Weber, *J. Phys. Chem. Lett.* **2016**, *7*, 2310.
[17] K. Katcko, E. Urbain, F. Ngassam, L. Kandpal, B. Chowrira, F. Schleicher, U. Halisdemir, D. Wang, T. Scherer, D. Mertz, B. Leconte, N. Beyer, D. Spor, P. Panissod, A. Boulard, J. Arabski, C. Kieber, E. Sternitzky, V. Da Costa, M. Hehn, F. Montaigne, A. Bahouka, W. Weber, E. Beaurepaire, C. Kübel, D. Lacour, M. Alouani, S. Boukari, M. Bowen, *Adv. Funct. Mater.* **2021**, *31*, 2009467.
[18] M. Campisi, R. Fazio, *Nat. Commun.* **2016**, *7*, 11895.
[19] G. Manzano, F. Galve, R. Zambrini, J. M. R. Parrondo, *Phys. Rev. E* **2016**, *93*, 052120.
[20] M. Serri, W. Wu, L. R. Fleet, N. M. Harrison, C. F. Hirjibehedin, C. W. M. Kay, A. J. Fisher, G. Aeppli, S. Heutz, *Nat. Commun.* **2014**, *5*, 3079.
[21] S. Tu, T. Ziman, G. Yu, C. Wan, J. Hu, H. Wu, H. Wang, M. Liu, C. Liu, C. Guo, J. Zhang, M. A. Cabero Z, Y. Zhang, P. Gao, S. Liu, D. Yu, X. Han, I. Hallsteinsen, D. A. Gilbert, M. Matsuo, Y. Ohnuma, P. Wölfle, K. L. Wang, J.-P. Ansermet, S. Maekawa, H. Yu, *Nat. Commun.* **2020**, *11*, 2023.
[22] P. N. Hai, S. Ohya, M. Tanaka, S. E. Barnes, S. Maekawa, *Nature* **2009**, *458*, 489.
[23] O. Hosten, N. J. Engelsen, R. Krishnakumar, M. A. Kasevich, *Nature* **2016**, *529*, 505.
[24] F. Schleicher, B. Taudul, U. Halisdemir, K. Katcko, E. Monteblanco, D. Lacour, S. Boukari, F. Montaigne, E. Urbain, L. M. Kandpal, J. Arabski, W. Weber, E. Beaurepaire, M. Hehn, M. Alouani, M. Bowen, *J. Phys. D: Appl. Phys.* **2019**, *52*, 305302.
[25] J. M. Teixeira, J. Ventura, J. P. Araujo, J. B. Sousa, P. Wisniowski, P. P. Freitas, *Appl. Phys. Lett.* **2010**, *96*, 262506.
[26] G.-X. Miao, J. Chang, B. A. Assaf, D. Heiman, J. S. Moodera, *Nat. Commun.* **2014**, *5*, 3682.
[27] Y. Lu, M. Tran, H. Jaffrã¨S, P. Seneor, C. Deranlot, F. Petroff, J.-M. George, B. Lépine, S. Ababou, G. Jézéquel, *Phys. Rev. Lett.* **2009**, *102*, 176801.
[28] M. Studniarek, U. Halisdemir, F. Schleicher, B. Taudul, E. Urbain, S. Boukari, M. Hervé, C.-H. Lambert, A. Hamadeh, S. Petit-Watelot, O. Zill, D. Lacour, L.-C. Joly, F. Scheurer, G. Schmerber, V. Da Costa, A. Dixit, P. Guitard, M. Acosta, F. Leduc, F. Choueikani, E. Otero, W. Wulfhekel, F. Montaigne, E. N. Monteblanco, J. Arabski, P. Ohresser, E. Beaurepaire, W. Weber, M. Alouani, et al., *Adv. Mater.* **2017**, *29*, 1606578.
[29] X. Chen, Y.-S. Fu, S.-H. Ji, T. Zhang, P. Cheng, X.-C. Ma, X.-L. Zou, W.-H. Duan, J.-F. Jia, Q.-K. Xue, *Phys. Rev. Lett.* **2008**, *101*, 197208.
[30] G. Francica, J. Goold, F. Plastina, M. Paternostro, *npj Quantum Inf* **2017**, *3*, 12.
[31] R. Landauer, *IBM J. Res. Dev.* **1961**, *5*, 183.
[32] E. Bormashenko, *Entropy* **2020**, *22*, 235.
[33] The antiferromagnetic superexchange interaction between Fe and Co mediated by the C60 molecule can be seen as two spinterfaces in series. This cancels the usual switch in sign of spin polarization across a spinterface.[16]
[34] E. Urbain, F. Ibrahim, M. Studniarek, F. N. Nyakam, L. Joly, J. Arabski, F. Scheurer, F. Bertran, P. Le Fèvre, G. Garreau, E. Denys, P. Wetzel, M. Alouani, E. Beaurepaire, S. Boukari, M. Bowen, W. Weber, *Adv. Funct. Mater.* **2018**, *28*, 1707123.
[35] Y. Takabayashi, K. Prassides, in *50 Years of Structure and Bonding – The Anniversary Volume*, Structure and Bonding (Ed.: D. M. P. Mingos), Vol. *172*, Springer International Publishing, London, UK **2016**, p. 119.
[36] K. Bader, M. Winkler, J. Van Slageren, *Chem. Commun.* **2016**, *52*, 3623.
[37] M. Gawełczyk, M. Krzykowski, K. Gawarecki, P. Machnikowski, *Phys. Rev. B* **2018**, *98*, 075403.
[38] We suppose here that the slower TF and SF strokes at the thicker C_{60} layer also respect this inequality.
[39] This internal check lends support of our educated guess for this structural geometry. See Experimental Section.
[40] A. Auffèves, *PRX Quantum* **2022**, *3*, 020101.
[41] S. Díaz, Á. S. Núñez, *J. Phys.: Condens. Matter* **2012**, *24*, 116001.
[42] J. D. V. Jaramillo, J. Fransson, *J. Phys. Chem. C* **2017**, *121*, 27357.
[43] S. L. Dudarev, G. A. Botton, S. Y. Savrasov, C. J. Humphreys, A. P. Sutton, *Phys. Rev. B* **1998**, *57*, 1505.
[44] I. E. Brumboiu, S. Haldar, J. Lüder, O. Eriksson, H. C. Herper, B. Brena, B. Sanyal, *J. Chem. Theory Comput.* **2016**, *12*, 1772.
[45] V. A. Basiuk, E. V. Basiuk, *Nanotubes Carbon Nanostruct.* **2017**, *25*, 410.
[46] L. Joly, B. Muller, E. Sternitzky, J.-G. Faullumel, A. Boulard, E. Otero, F. Choueikani, J.-P. Kappler, M. Studniarek, M. Bowen, P. Ohresser, *J. Synchrotron Radiat.* **2016**, *23*, 652.